Structure and selectivity engineering of the M₁ muscarinic receptor toxin complex

Shoji Maeda[1,*], **Jun Xu**[2], **Francois Marie N. Kadji**[3], **Mary J. Clark**[4], **Jiawei Zhao**[5], **Naotaka Tsutsumi**[1,6,7], **Junken Aoki**[3], **Roger K. Sunahara**[4], **Asuka Inoue**[3], **K Christopher Garcia**[1,6,7], **Brian K. Kobilka**[1,2,*]

[1]Department of Molecular and Cellular Physiology, Stanford University School of Medicine, Stanford, CA 94305, USA

[2]Beijing Advanced Innovation Center for Structural Biology, School of Life Science, Tsinghua University, Beijing, China

[3]Graduate School of Pharmaceutical Science, Tohoku University, Sendai, Japan

[4]Department of Pharmacology, University of California San Diego School of Medicine, La Jolla, CA 92093, USA

[5]Tsinghua-Peking Joint Center for Life Sciences, School of Life Sciences, Tsinghua University, Beijing, China

[6]Department of Structural Biology, Stanford University School of Medicine, Stanford, CA 94305, USA

[7]Howard Hughes Medical Institute, Stanford University School of Medicine, Stanford, CA 94305, USA

Abstract

Muscarinic toxins (MTs) are natural toxins produced by mamba snakes that primarily bind to muscarinic acetylcholine receptors (MAChRs) and modulate their function. Despite their similar primary and tertiary structures, MTs show distinct binding selectivity toward different MAChRs. The molecular details of how MTs distinguish MAChRs are not well understood. Here, we present the crystal structure of M₁AChR in complex with MT7, a subtype-selective anti-M₁AChR snake venom toxin. The structure reveals the molecular basis of the extreme subtype specificity of MT7

---

for M_1AChR and the mechanism by which it regulates receptor function. Through in vitro engineering of MT7 finger regions that was guided by the structure, we have converted the selectivity from M_1AChR toward M_2AChR, suggesting that the three-finger fold is a promising scaffold for developing G protein–coupled receptor modulators.

Selective targeting of a specific subtype of a G protein–coupled receptor (GPCR) among its family members is a major challenge in developing receptor-specific drugs with minimal undesired effects (1). Efforts to design compounds with strict specificity toward target GPCRs are often hampered by high conservation of the orthosteric binding site. Allosteric binding sites, on the other hand, share less homology between family members and thus have been targeted as alternative sites for drug discovery (2,3). Muscarinic toxins (MTs) are small protein toxins consisting of 65 to 66 amino acid residues derived from the venoms of African mambas. They belong to a large superfamily, the three-finger toxin (3FT) family (4–6). Despite their high similarity in the sequence and structure, 3FTs exhibit distinct interaction profiles against the five muscarinic acetylcholine receptor (MAChR) subtypes (M_1AChR to M_5AChR) (7–11). Among the subtypes, MT7 has the highest specificity toward M_1AChR over other muscarinic receptors, with a difference in affinity of more than five orders of magnitude (12–16). Studies have shown that MT7 binds M_1AChR at subnanomolar affinity with a very slow dissociation rate (17), inhibits agonist-mediated guanosine $5'$-O-($3'$-thiotriphosphate)(GTP-γ-S) binding and downstream signaling (16,18–20), and decreases the dissociation rate of orthosteric antagonists $\{[^3H]N$-methylscopolamine ([^3H]NMS) or [^3H]pirenzepine$\}$(20). Thus, MT7 is a potent negative allosteric modulator (NAM) for M_1AChR activation and a positive allosteric modulator (PAM) for antagonist binding. Because of its extremely high specificity toward M_1AChR, MT7 has attracted research interest into understanding the structural basis for its mode of action. Here, we present the crystal structure of the MAChR-MT7 complex bound to the orthosteric antagonist. The structure reveals the molecular mechanism of the allosteric regulation by MT7 as well as the specific interactions that dictate subtype selectivity. On the basis of this structural information, we engineered MT7 in vitro to redirect its selectivity, yielding a modulator specific for M_2AChR. More broadly, this work shows the utility of the 3FT fold for solving the difficult problem of generating specific high-affinity binding proteins to GPCR extracellular loops.

Preparation and structure determination of the M1AChR-MT7 complex

The M_1AChR-MT7 complex was formed by using recombinantly expressed M_1AChR from Sf9 insect cells and MT7 from Hi5 insect cells as described in the supplementary materials (fig. S1A). Although we were able to form a stable complex between M_1AChR bound to the antagonist atropine and MT7 (fig. S1B), our initial attempts to crystallize this complex in lipidic cubic phase (LCP), a widely used method for crystallizing GPCRs, were unsuccessful, yielding crystals made of M_1AChR alone. It has been shown that low–molecular weight polyethylene glycols (PEGs), reagents commonly used as precipitants in LCP crystallography, can occupy the extracellular vestibule of M_4AChR (21). We determined that low–molecular weight PEGs could compete with MT7 for binding to M_1AChR (fig. S1, C and D), supporting the notion that MT7 is displaced by the PEG

molecules during crystallogenesis. Through the screening of alternative precipitant reagents, we finally succeeded in obtaining crystals of the M_1AChR-MT7 complex by using the hanging drop vapor diffusion method in a condition with no PEG, and the structure was determined at 2.55-Å resolution (fig. S2 and table S1).

Interactions between M_1AChR and MT7

The structure shows that the extracellular vestibule is occupied, with finger loop 2 blocking access to the orthosteric site (Fig. 1A and fig. S3), and this explains the reported slow dissociation of [^{3}H]NMS from the orthosteric site when bound to MT7 (18). Comparison of showed that finger loops 1 and 3 undergo large showed that finger loops 1 and 3 undergo large structural rearrangements upon binding to M_1AChR, facilitating extensive interactions with the receptor, while finger loop 2 is mostly unchanged (22) (fig. S4). The large displacement of finger loops 1 and 3 is consistent with molecular dynamics simulations on another snake-derived 3FT, toxin α from *Naja nigiicollis* (23), which revealed finger loops 1 and 3 to be highly dynamic. The flexibility of finger loops 1 and 3 may explain why some 3FTs can bind to multiple targets (24). In agreement with previous studies, the interactions between M_1AChR and MT7 occur predominantly with extracellular loop 2 (ECL2) M_1AChR (Fig. 1B) (25–27). Finger loop 1 of MT7 forms extensive hydrophobic interactions with residues in transmembrane helix 4 (TM4) and ECL2 (Fig. 1B, red rectangle). Because these hydrophobic residues are conserved in finger loop 1 of other MT members and in TM4 and ECL2 of other muscarinic receptor subtypes (Fig. 1B and fig. S5), these interactions are not likely to contribute to MT7 subtype selectivity. Finger loop 2 forms the most extensive interactions with ECL2 and TM7, largely consisting of polar contacts. Residues in finger loops 2 and 3 form specific interactions with M_1Clh residues E170 and L174 in ECL2 and E397$^{7.32}$ and E401$^{7.36}$ at the top of TM7 [superscripts correspond to Ballesteros-Weinstein numbering (28)] (Fig. 1B, yellow and cyan rectangles). Sequence alignment of MAChRs shows that E170, L174, E397$^{7.32}$, and E401$^{7.36}$ are not conserved in other MAChRs, suggesting that these M_1AChR-specific interactions likely dictate the subtype selectivity of MT7 (Fig. 1B). This conclusion is supported by studies where substitution of these residues of M_1AChR into the equivalent positions in M_3AChR or M_5AChR yields receptors that bind MT7 (25,26,29). Not surprisingly, these subtype-specific residues engaged in MT7 binding also form part of the binding pocket of M_1AChR-selective small-molecule allosteric modulators (30–32).

Structural changes in M_1AChR stabilized by MT7

When superposing M_1AChR-MT7 bound to atropine and toxin-free M_1AChR bound to tiotropium, engagement of MT7 stabilizes a 3- to 4-Å outward movement of TM6, ECL3, and TM7 due to the insertion of finger loop 2 into the extracellular vestibule (Fig. 2A). The outward displacement of TM7 is stabilized by a polar network involving E401$^{7.36}$ and Y82$^{2.61}$ in M_1AChR and R34 from the tip of finger loop 2 (Figs. 1B and 2B). This tyrosine residue, together with Y85$^{2.64}$, which is located one helical turn above Y82$^{2.61}$, has been reported to be one of the key elements for the binding of allosteric compounds (31, 33). In addition, Y51 and R52 in finger loop 3 form polar interactions with E397$^{7.31}$ (Fig. 2B). These interactions position P33 in finger loop 2 to interact with the backbone and side

chains of W400[7.35] and E401[7.36] of TM7, displacing it outward. The outward movement of W400[7.35] at the top of TM7 in turn stabilizes the outward displacement of TM6 through interactions with M384[6.54] (Fig. 2B and fig. S6). A tryptophan residue at position 7.35 (W[7.35]) has been identified as a critical residue for the binding of small-molecule allosteric modulators in M_1AChR (30–32) and M_2AChR (34). These residues in the active MAChRs undergo inward displacement, and W[7.35] forms an aromatic stacking interaction with a PAM, LY2119620, in M_2AChR (35, 36). Therefore, W[7.35] plays a role in both the positive and negative allosteric modulation of MAChRs by stabilizing the extracellular side of TM6 either inward or outward, respectively (Fig. 2B and fig. S6). We recently reported the active-state structure of M_1AChR in complex with the G protein G_{11} (36). In this structure, there is a 5.7-Å inward movement at the extracellular end of TM6 (at the α carbon of F390) relative to the inactive-state M_1AChR, which is accompanied by an outward movement of the cytoplasmic side of TM6 (Fig. 2C). In contrast, the outward movement of the extracellular end of TM6 in the M_1AChR-MT7 structure is associated with a small inward movement of the cytoplasmic end of TM6 (Fig. 2, B and C). The allosteric coupling of the extracellular and intracellular ends of TM6 can be explained by a rigid body movement which pivots around W378[6.48], the "rotamer toggle switch" (37)(Fig. 2C). As a result of the inward displacement of the cytoplasmic end of TM6 in the M_1AChR-MT7 complex, R123[3.50] in the DRY motif forms polar interactions with N60[2.39] from TM2 and the backbone carbonyl of A363[6.33] from TM6 (Fig. 2B). These interactions enhance the tight interhelical packing and lock the receptor in the inactive state. The extracellular end of TM5 is displaced slightly inward in the M_1AChR-MT7 complex compared with its position in the tiotropium-bound state (Fig. 2A). Unlike displacements of TM6 and TM7 helices that are stabilized by MT7, the displacement of TM5 could be attributed to the different sizes of the orthosteric antagonists. Atropine has a single phenyl group that faces TM3 and TM4, whereas tiotropium has two ring systems (2-thienyl groups), with the second ring facing TM5 (fig. S7). The lack of the second ring in atropine likely allows the slight inward displacement of TM5 relative to the position in the tiotropium-bound state. Indeed, the superposition of the tiotropium into the orthosteric binding site of the atropine-bound state makes a steric clash with T192[5.42] (fig. S7).

Redirecting the subtype selectivity of MT7 from M_1AChR to M_2AChR

With its small size and high stability, the 3FT fold has been utilized as an alternative scaffold to generate protein binders (38, 39). Therefore, we designed a phage display library using MT7 as a template scaffold to explore whether we could redirect the specificity to other muscarinic receptor subtypes through structure-guided engineering. On the basis of the residues of MT7 in contact with M_1AChR in the crystal structure, we selected residues from each finger loop to be randomized (fig. S8). For the target molecule, we used M_2AChR in the presence of the antagonist atropine. After four rounds of phage panning, we identified clone 24, which binds subtype selectively toward M_2AChR over M_1AChR and has conformational selectivity toward the inactive state (Fig. 3, A and B). Moreover, it confers a slow dissociation of the antagonist [³H]NMS from the orthosteric binding pocket (Fig. 3C), suggesting that it binds allosterically to the extracellular vestibule. A substoichiometric amount of clone 24 in the pull-down assay suggested a weak affinity of the engineered toxin

for M_2AChR. We therefore performed affinity maturation by introducing random mutations throughout the toxin coding region and selection using yeast surface display to obtain a high-affinity variant (fig. S9). High-affinity binders were enriched using progressively lower concentrations of M_2AChR bound with atropine during selections. After two rounds of magnetic-activated cell sorting, we further performed fluorescence-activated cell sorting (FACS) to select high-affinity clones. By combining the consensus mutations from randomly selected sequences of the affinity-matured clones, we created a high-affinity variant, Tx24 (Fig. 3D). Tx24 gained a 30-fold enhancement in affinity for M_2AChR over clone 24 (Fig. 3E) and retained the same subtype and conformation selectivity as the original clone 24 (Fig. 3, F and G). Figure S10 shows the sequence alignments for MT7, clone 24, and Tx24.

Functional characterization of Tx24 on M_2AChR and other GPCRs

We subsequently investigated the pharmacological properties of Tx24. In the radioligand dissociation assay, Tx24 substantially decreased the dissociation rate of $[^3H]NMS$ from M_2AChR, in accordance with the properties of the original clone 24 (Fig. 4). In contrast, Tx24 showed little or no impact on the dissociation rate of antagonists from other MAChR family members or from the β_2-adrenergic receptor (β_2AR) (Fig. 4A and fig. S11A), confirming the high subtype specificity of Tx24. A small (1.8-fold) decrease in the dissociation rate of $[^3H]NMS$ in M_1AChR is likely caused by the residual binding between Tx24 and M_1AChR that was observed in the pull-down assay. However, this effect was much smaller than that for M_2AChR, for which a >700-fold decrease in off-rate was observed in the presence of Tx24 (fig. S11A). Moreover, the affinity of $[^3H]NMS$ for M_2AChR became substantially higher in the presence of Tx24 (Fig. 4B), whereas enhancement of $[^3H]NMS$ binding was barely detectable in M_1AChR and absent in M_4AChR, confirming the specificity of Tx24 for M_2AChR (fig. S11B). The median effective concentration of Tx24 for this effect on M_2AChR is in good agreement with the on-yeast affinity measurement (Fig. 3E and fig. S11B). Apart from the substantial influence on the behavior of antagonists, Tx24 has a slight negative allosteric effect on the potency of ACh, suggesting that it is a weak NAM for agonists (Fig. 4C). Next, we investigated the effect of Tx24 on G protein activation using the NanoBiT system (40). In the NanoBiT system, MAChR-dependent cognate G protein activation is monitored through the decrease of the luminescence signal due to the heterotrimer dissociation (fig. S12A). Tx24 on its own showed no agonistic or antagonistic activity (fig. S12A). When these results were taken together, Tx24 enhanced the inhibition by the antagonist atropine and this enhancement was specific for M_2AChR (Fig. 5A and table S2). In contrast, we observed no impact on G protein activation from other MAChRs or from the μ-opioid receptor or β_2AR (Fig. 5A and fig. S12). These results further validate the M_2AChR subtype selectivity of Tx24 in a cellular signaling context.

Probe-dependent positive allosteric modulation of Tx24

Probe dependency of the allosteric modulator in M_2AChR has been reported with a PAM molecule for agonists that implicates a complex interaction between orthosteric and allosteric binding sites (41). To determine the probe dependency of Tx24, we assessed three orthosteric antagonist compounds: atropine, NMS, and tiotropium. Although Tx24 enhanced

the inhibition of M_2AChR activity by atropine or NMS, it had no impact on the inhibition by tiotropium (Fig. 5B and table S3), indicating that Tx24 is a probe-selective PAM for atropine and NMS. Recent structural dynamics analysis by nuclear magnetic resonance (NMR) spectroscopy revealed distinct conformations of M_2AChR for NMS- and tiotropium-bound states (42). Atropine and NMS share a similar structure with a single ring system, whereas tiotropium has two rings (Fig. 5B). The preferential allosteric effects of Tx24 for these smaller antagonists are likely due to the fact that it was developed against atropine-bound M_2AChR. Consistent with this notion, Tx24 has a higher affinity for M_2AChR bound to NMS than for M_2AChR bound to tiotropium (fig. S13).

Effect of Tx24 binding on conformation of M_2AChR

To assess the allosteric structural changes resulting from Tx24, we labeled $T386^{6.34}$ at the cytoplasmic end of TM6 with monobromobimane (mBBr) and introduced a tryptophan mutation at $S210^{5.62}$, which upon activation of the receptor quenched the fluorescence emitted from mBBr on TM6 (fig. S14). Compared with the apo state, the ACh-activated state had a significantly lower fluorescence intensity, which was further decreased in the presence of an intracellular G protein–mimetic nanobody, Nb9–8, whereas there was only a small decrease in fluorescence in the atropine-bound or Tx24-bound state (Fig. 6A). There was little change in the fluorescence intensity in the presence of both atropine and Tx24 regardless of the order of addition. When the receptor was first incubated with ACh, the addition of Tx24 resulted in only a small increase in fluorescence. However, when the receptor was first incubated with Tx24, the addition of ACh did not reduce the fluorescence. These results are consistent with the observation that Tx24 binds with lower affinity to ACh-bound M_2AChR (Fig. 3G) and, therefore, cannot stabilize an inactive conformation in TM6. Notably, the receptor remains in the active conformation in the presence of Nb9–8 regardless of the presence of Tx24 or the order of addition of these components.

The structural impact of Tx24 on M_2AChR conformation and dynamics was further investigated by solution NMR spectroscopy using methionine residues as conformational probes (42). The labeled methionines are well-positioned to detect conformational changes in the extracellular vestibule ($M406^{6.54}$), the orthosteric binding pocket ($M77^{2.58}$), the transduction core ($M112^{3.41}$), the junction of ICL2 and TM4 ($M143^{4.45}$), and the cytoplasmic ends of TM5 and TM6 ($M202^{5.54}$) (fig. S15). On the basis of the structure of M_1AChR-MT7, we would not expect Tx24 to directly interact with any of the methionine probes. Binding of Tx24 caused chemical shift perturbations of $M77^{2.58}$, $M202^{5.54}$ and $M406^{6.54}$ in the heteronuclear single-quantum coherence (HSQC) spectra among the five labeled methionines (Fig. 6, B to E). $M77^{2.58}$ underwent substantial changes in chemical shift and peak pattern upon binding to Tx24 compared with the apo or atropine-bound state, suggesting distinct local conformations and dynamics stabilized by Tx24. Co-incubation with atropine had no further influence on the $M77^{2.58}$ peak, which indicated that the conformation of the extracellular side of TM2 is mostly dominated by Tx24. $Y80^{2.61}$ and $Y83^{2.64}$, both located above $M77^{2.58}$, play pivotal roles in the allosteric transmission of structural changes in the extracellular vestibule to the orthosteric pocket (31, 33). It is possible that Tx24 triggers a conformational change around $Y80^{2.61}$ in M_2AChR that is similar to the change we observed around the analogous $Y82^{2.61}$ residue in the M_1AChR-

MT7 complex (Fig. 2B), and this conformational change is reported by M77[2.58] in the HSQC spectra. Although the M202[5.54] and M406[6.54] peak profiles showed little change from apo state to atropine-bound state, their positions shifted markedly upon binding with Tx24 (Fig. 6F). M406[6.54] is located in close contact with W422[7.35], which faces the extracellular vestibule in the inactive state (Fig. 6G). Given the size of Tx24, it is likely that it interacts with W422[7.35] and provides M406[6.54] with a different microenvironment in the apo state and the atropine-bound state. Unlike M77[2.58] and M406[6.54], M202[5.54] is located at the TM5-TM6 interface on the intracellular side of the receptor and away from the putative Tx24 binding pocket (Fig. 6G). The spectral changes observed in M202[5.54] indicate that the extracellular conformational change induced by Tx24 propagates to the intracellular region and allosterically stabilizes a distinct intracellular conformation of the TM5-TM6 interface from the apo or atropine-bound state. Both M202[5.54] and M406[6.54] peaks further shift when co-incubated with atropine (Fig. 6F), indicating a cooperative action between Tx24 and atropine, as evident from the pharmacological response (Fig. 5G).

Discussion

Natural organisms such as plants, bacteria, fungi, and animals have developed various molecules for their survival: for self-defense against predators and for capturing prey. These molecules have been a rich source of drugs and tool compounds for a diverse range of targets, including GPCRs (43). Whereas small molecules dominate the pharmacopeia for GPCRs, there is growing interest in peptides and small proteins because of their potential to be highly selective. The structure of M_1AChR -MT7 reveals the molecular basis for its strict subtype selectivity and also how the conformational changes of M_1AChR upon MT7 binding lead to inactivation of the receptor. The ability to redirect its MAChR subtype preference through in vitro protein evolution demonstrates the promise of the 3FT fold as an alternative scaffold for generating protein-based modulators.

Supplementary Material

Refer to Web version on PubMed Central for supplementary material.

ACKNOWLEDGMENTS

Data and materials availability:

The atomic coordinates of M_1AChR-MT7 have been deposited in the RCSB Protein Data Bank (PDB) with the identifier 6WJC. Materials for these engineered toxins are available from the corresponding authors upon request. Expression plasmids for the NanoBiT-G-protein dissociation assay are available from A.I. under a material transfer agreement with Tohoku University.

REFERENCES AND NOTES

1. Lee S-M, Booe JM, Pioszak AA, Eur. J. Pharmacol. 763, 196–205 (2015). [PubMed: 25981303]

2. Christopoulos A, Mol. Pharmacol. 86, 463–478 (2014). [PubMed: 25061106]

3. Langmead CJ, Christopoulos A, Curr. Opin. Cell Biol. 27, 94–101 (2014). [PubMed: 24680434]

4. Kessler P, Marchot P, Silva M, Servent D, J. Neurochem 142 (suppl. 2), 7–18 (2017). [PubMed: 28326549]

5. Ségalas I et al., Biochemistry 34, 1248–1260 (1995). [PubMed: 7827075]

6. Liang JS et al., Toxicon 34, 1257–1267 (1996). [PubMed: 9027981]

7. Bradley KN, Pharmacol. Ther. 85, 87–109 (2000). [PubMed: 10722122]

8. Karlsson E, Jolkkonen M, Mulugeta E, Onali P, Adem A, Biochimie 82, 793–806 (2000). [PubMed: 11086210]

9. Jerusalinsky D et al., Toxicon 38, 747–761 (2000). [PubMed: 10695963]

10. Servent D et al., Toxicon 58, 455–463 (2011). [PubMed: 21906611]

11. Servent D, Fruchart-Gaillard C, J. Neurochem. 109, 1193–1202 (2009). [PubMed: 19457160]

12. Max SI, Liang JS, Potter LT, J. Neurosci. 13, 4293–4300 (1993). [PubMed: 8410188]

13. Max SI, Liang JS, Potter LT, Mol. Pharmacol. 44, 1171–1175 (1993). [PubMed: 8264554]

14. Max SI, Liang JS, Valentine HH, Potter LT, J. Pharmacol. Exp. Ther. 267, 480–485 (1993). [PubMed: 8229778]

15. Carsi JM, Potter LT, Life Sci. 68, 2541–2547 (2001). [PubMed: 11392624]

16. Näsman J, Jolkkonen M, Ammoun S, Karlsson E, Åkerman KEO, Biochem. Biophys. Res. Commun. 271, 435–439 (2000). [PubMed: 10799315]

17. Krajewski JL, Dickerson IM, Potter LT, Mol. Pharmacol. 60, 725–731 (2001). [PubMed: 11562434]

18. Olianas MC et al., Br. J. Pharmacol. 131, 447–452 (2000). [PubMed: 11015294]

19. Bradley KN, Rowan EG, Harvey AL, Toxicon 41, 207–215 (2003). [PubMed: 12565740]

20. Olianas MC, Adem A, Karlsson E, Onali P, Eur. J. Pharmacol. 487, 65–72 (2004). [PubMed: 15033377]

21. Thal DM et al., Nature 531, 335–340 (2016). [PubMed: 26958838]

22. Fruchart-Gaillard C et al., Mol. Pharmacol. 74, 1554–1563 (2008). [PubMed: 18784346]

23. Gilquin B et al., Protein Sci. 12, 266–277 (2003). [PubMed: 12538890]

24. Blanchet G et al., Biochimie 103, 109–117 (2014). [PubMed: 24793485]

25. Kukkonen A, Peräkylä M, Åkerman KEO, Näsman J, J. Biol. Chem. 279, 50923–50929 (2004). [PubMed: 15452105]

26. Rondinelli S, Näreoja K, Näsman J, Toxins 3, 1393–1404 (2011). [PubMed: 22174976]

27. Marquer C et al., J. Biol. Chem. 286, 31661–31675 (2011). [PubMed: 21685390]

28. Ballesteros JA, Weinstein H, in Receptor Molecular Biology, vol. 25 of Methods in Neurosciences, Sealfon SC, Ed. (Academic Press, 1995), pp. 366–428.

29. Xu J et al., J. Mol. Recognit. 28, 239–252 (2015). [PubMed: 25683330]

30. Abdul-Ridha A et al., J. Biol. Chem. 289, 6067–6079 (2014). [PubMed: 24443568]

31. Abdul-Ridha A et al., J. Biol. Chem. 289, 33701–33711 (2014). [PubMed: 25326383]

32. Ma L et al., Proc. Natl. Acad. Sci. U.S.A. 106, 15950–15955 (2009). [PubMed: 19717450]

33. Hollingsworth SA et al., Nat. Commun. 10, 3289 (2019). [PubMed: 31337749]

34. Dror RO et al., Nature 503, 295–299 (2013). [PubMed: 24121438]

35. Kruse AC et al., Nature 504, 101–106 (2013). [PubMed: 24256733]

36. Maeda S, Qu Q, Robertson MJ, Skiniotis G, Kobilka BK, Science 364, 552–557 (2019). [PubMed: 31073061]

37. Visiers I, Ballesteros JA, Weinstein H, Methods Enzymol. 343, 329–371 (2002). [PubMed: 11665578]

38. Naimuddin M et al., Mol. Brain 4, 2 (2011). [PubMed: 21214917]

39. Cai W et al., J. Recept. Signal Transduct. 34, 154–161 (2014).

40. Inoue A et al., Cell 177, 1933–1947.e25 (2019). [PubMed: 31160049]

41. Valant C, Felder CC, Sexton PM, Christopoulos A, Mol. Pharmacol. 81, 41–52 (2012). [PubMed: 21989256]

42. Xu J et al., Mol. Cell 75, 53–65.e7 (2019). [PubMed: 31103421]

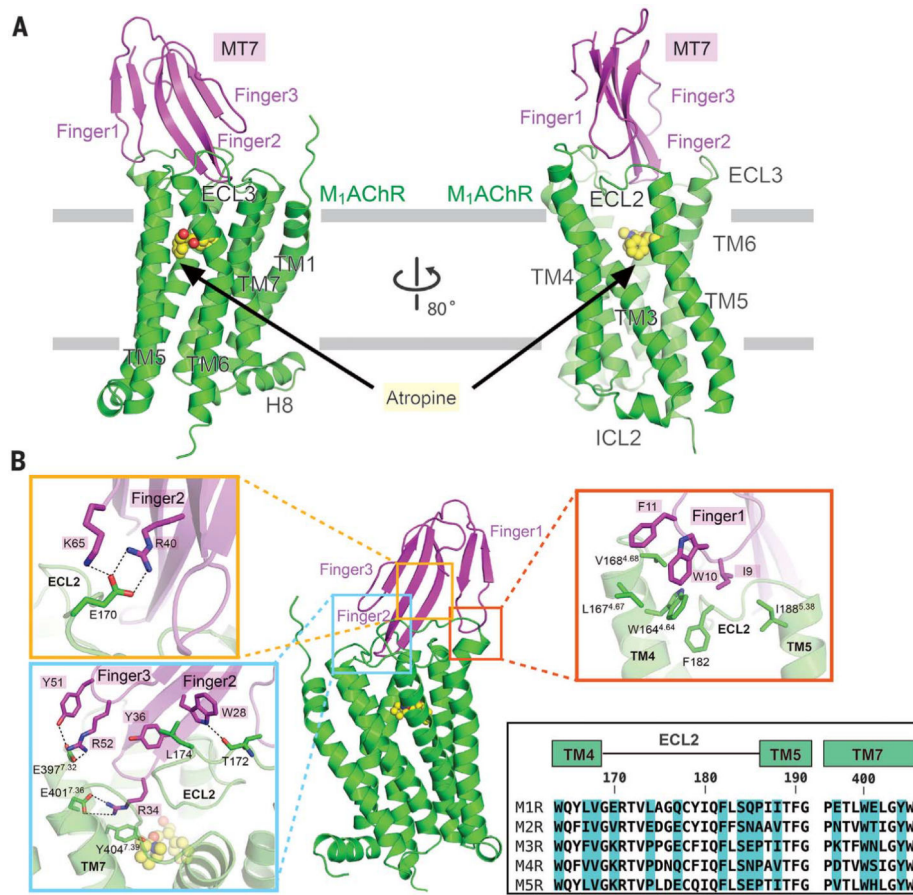43. Muratspahic E, Freissmuth M, Gruber CW, Trends Pharmacol. Sci. 40, 309–326 (2019). [PubMed: 30955896]

Fig. 1. Structure of the M$_1$AChR-MT7 complex.
(**A**) Side view of the overall structure of M$_1$AChR-MT7. For clarity, T4L fused to M$_1$AChR was removed from the structure. MT7 and M$_1$AChR are colored magenta and green, respectively. The orthosteric antagonist atropine is colored yellow. Finger loops 1 to 3 of MT7 and ECLs and TM helices of M$_1$AChR are labeled. (**B**) Detailed interactions between finger loops of MT7 and M$_1$AChR. Interactions with finger loop 1 (red rectangle) and finger loops 2 and 3 (cyan and orange rectangles) are featured in enlarged views. Side chains making interactions are depicted as sticks. Sequence alignments of TM4-ECL2-TM5 and ECL3-TM7 from the five MAChR subtypes are shown in the bottom box. Residue numbers and TM helices of M$_1$AChR are represented above the alignment. Amino acid residues interacting with MT7 in M$_1$AChR are highlighted in blue. Single-letter abbreviations for the amino acid residues are as follows: A, Ala; C, Cys; D, Asp; E, Glu; F, Phe; G, Gly; H, His; I, Ile; K, Lys; L, Leu; M, Met; N, Asn; P, Pro; Q, Gln; R, Arg; S, Ser; T, Thr; V, Val; W, Trp; and Y, Tyr.
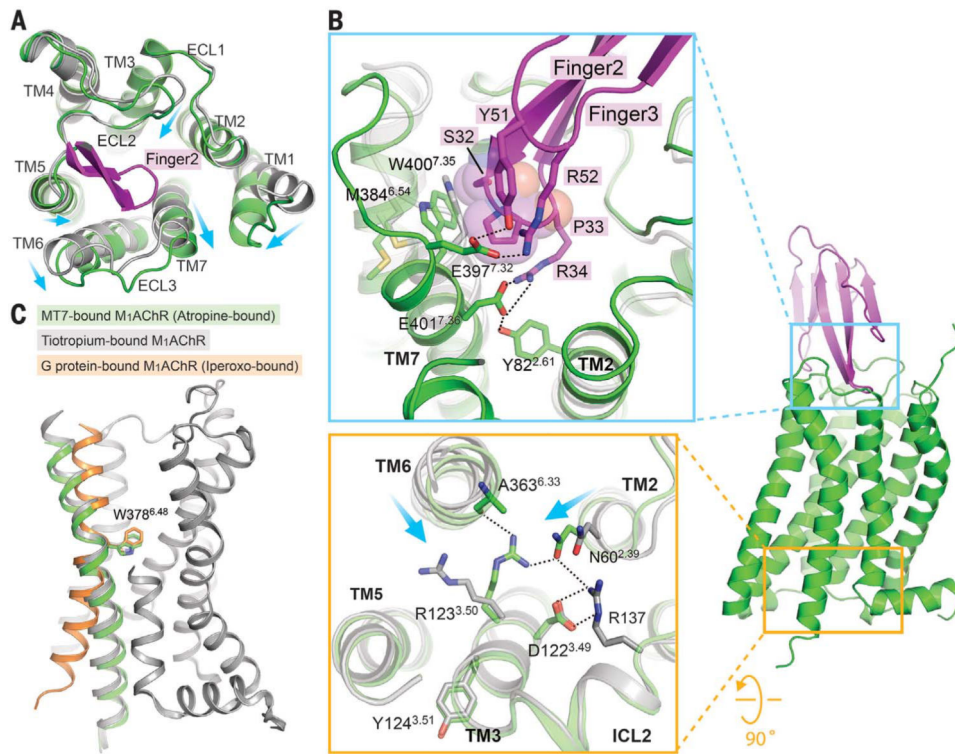
Fig. 2. Conformational changes in M_1AChR stabilized by MT7 binding.

(**A**) Superposition of tiotropium-bound M_1AChR (gray; PDB ID 5CXV) and atropine-bound M_1AChR-MT7 complex (green) from the extracellular view. Part of finger loop 2 that interacts with TM7 is shown (magenta). Conformational changes are shown with arrows. (**B**) (Top) Insertion of finger loop 2 stabilizes conformational changes at the extracellular side of TM2, TM6, and TM7. Note that P33 from MT7, represented as spheres, stabilizes W400 outward. (Bottom) Differences in the organization of the DRY motif in the M_1AChR-MT7 complex compared with that of tiotropium-bound M_1AChR. Displacements of TM helices 2 and 6 are shown with arrows. (**C**) Conformational change of TM6 between different states of M_1AChR, with W378 serving as a pivotal position: M_1AChR from the M_1AChR-MT7 complex (green); M_1AChR from the tiotropium-bound inactive state (gray; PDB ID 5CXV), and M_1AChR from the M_1AChR-G_{11} complex (orange; PDB ID 6OIJ).
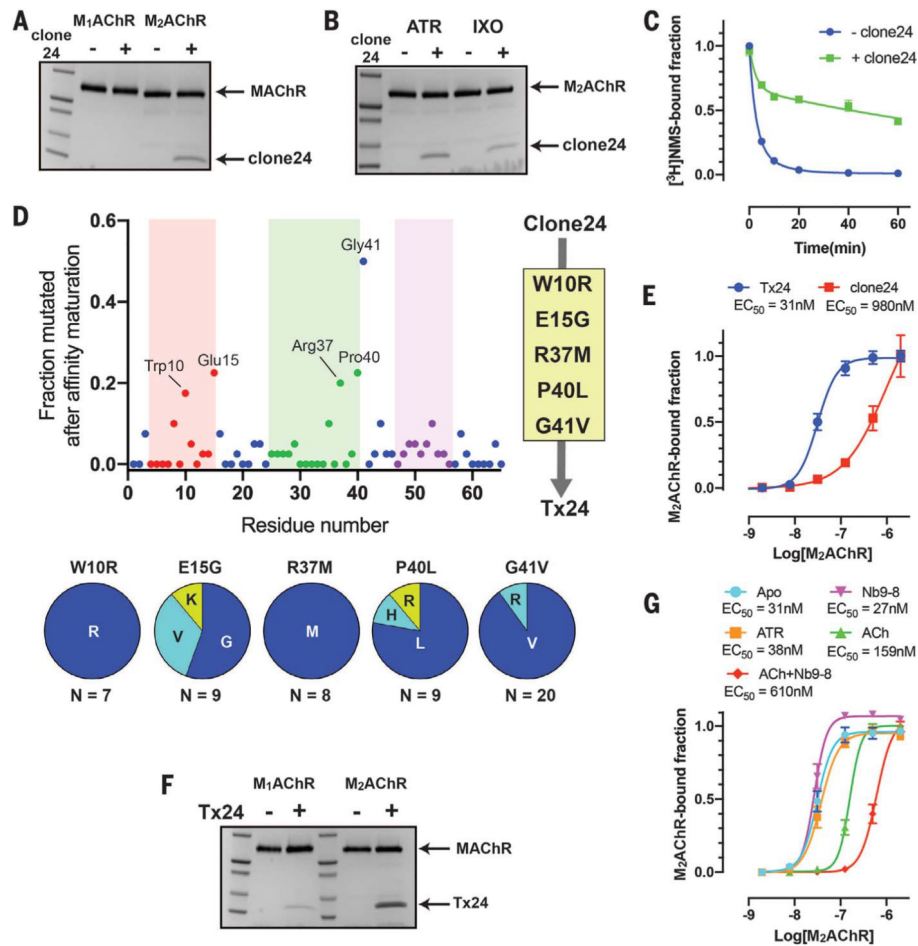
Fig. 3. Identification and affinity maturation of a subtype-selective M₂AChR allosteric modulator through in vitro selection.

(**A**) Pull-down assay showing that clone 24 binds subtype selectively to M₂AChR over M₁AChR. The experiment was carried out in the presence of 10 μM atropine. (**B**) Pull-down assay showing the conformation preference of clone 24 toward the atropine (ATR)–bound state over the iperoxo (IXO)–bound state of M₂AChR. (**C**) Comparison of the dissociation kinetics of the orthosteric antagonist [^{3}H]NMS from M₂AChR in the clone 24–bound and apo state. Data represent means ± SEM of three experiments performed in triplicate. (**D**) Sequence analysis of 50 randomly selected clones after the second FACS enrichment. The finger loop regions 1, 2, and 3 are colored red, green, and purple, respectively. The five most frequent mutations (W10R, E15G, R37M, P40L, and G41V) were combined into clone 24 to generate Tx24. (**E**) Comparison of the affinities of clone 24 and Tx24 to M₂AChR using on-yeast affinity measurement in the presence of 10 μM atropine. Data represent means ± SEM of three independent experiments. (**F**) Pull-down assay of Tx24 using M₁AChR or M₂AChR in the presence of 10μM atropine. Tx24 prefers M₂AChR over M₁AChR. (**G**) Comparison of the affinity of Tx24 for M₂AChR bound to different ligands alone or in combination with a G protein mimetic nanobody using on-yeast affinity measurement. Symbols and error bars represent means and SEM of three independent experiments.
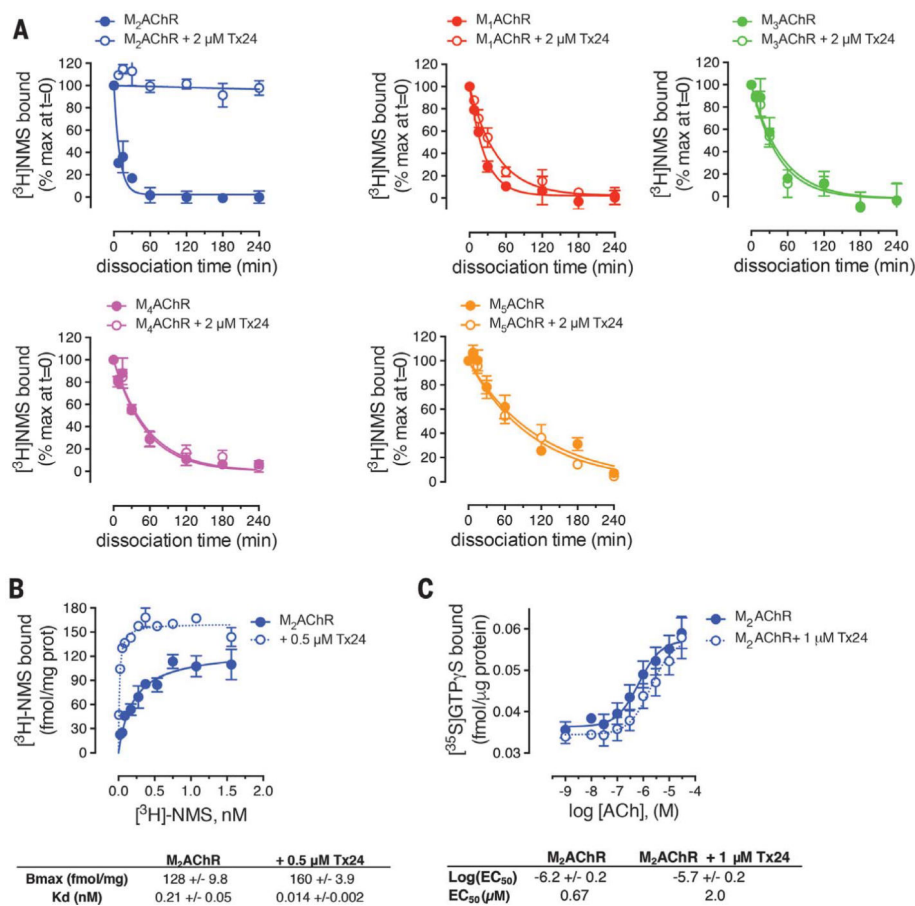
Fig. 4. Pharmacological impact of Tx24 for the dissociation of the orthosteric antagonist.
(**A**) Comparison of the [^{3}H]NMS dissociation kinetics from M$_2$AChR (blue), M$_1$AChR (red), M$_3$AChR (magenta), M$_4$AChR (green), or M$_5$AChR (orange) in the absence (filled symbols, solid line), or presence (empty symbol, solid line) of 2 μM Tx24. Shown are the combined results from four assays performed in duplicate. (**B**) Saturation binding of [^{3}H]NMS to M$_2$AChR in the absence (filled symbol, solid line) or presence (empty symbol, dotted line) of 0.5 μM Tx24 after 24-hour incubation. Shown are the combined results from four assays performed in duplicate. (**C**) ACh-stimulated [^{35}S]GTP-γ-S binding at M$_2$AChR expressed in CHO cells in the absence (filled symbol, solid line) or presence (empty symbol, dotted line) of 1 μM Tx24. Symbols and error bars represent means and SEM of the combined results from three or four assays performed in duplicate.
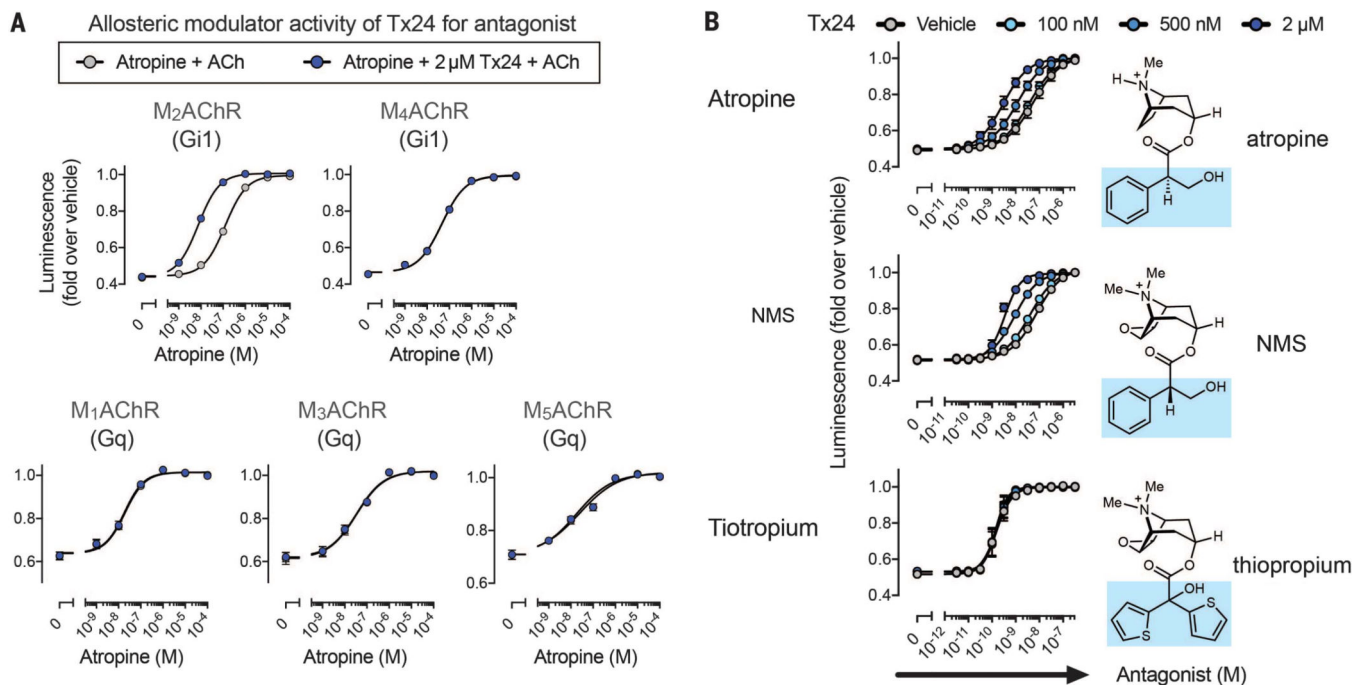
Fig. 5. Tx24 is a probe-selective PAM for antagonists.
(**A**) Allosteric modulator activity of Tx24 toward antagonist atropine. The cells expressing the NanoBiT–G protein and the test GPCR were treated with titrated atropine followed by addition of Tx24 or vehicle. Luminescent signals were measured before and after ligand stimulation (10 μM ACh). (**B**) HEK293 cells transiently expressing the NanoBiT-G_{i1} protein and M_2AChR were loaded with coelenterazine and pretreated with titrated antagonist (atropine, NMS, or tiotropium), followed by addition of Tx24 (100 nM, 500 nM, or 2 μM). Luminescent signals were measured before and after ACh treatment (10 μM). Changes in luminescent signals were normalized to those with vehicle treatment. The chemical structure of each antagonist compound is placed next to the respective curve, with the aromatic head group highlighted in blue. Symbols and error bars represent means and SEM of three to five independent experiments, each performed in duplicate (see tables S2 and S3 for statistics).
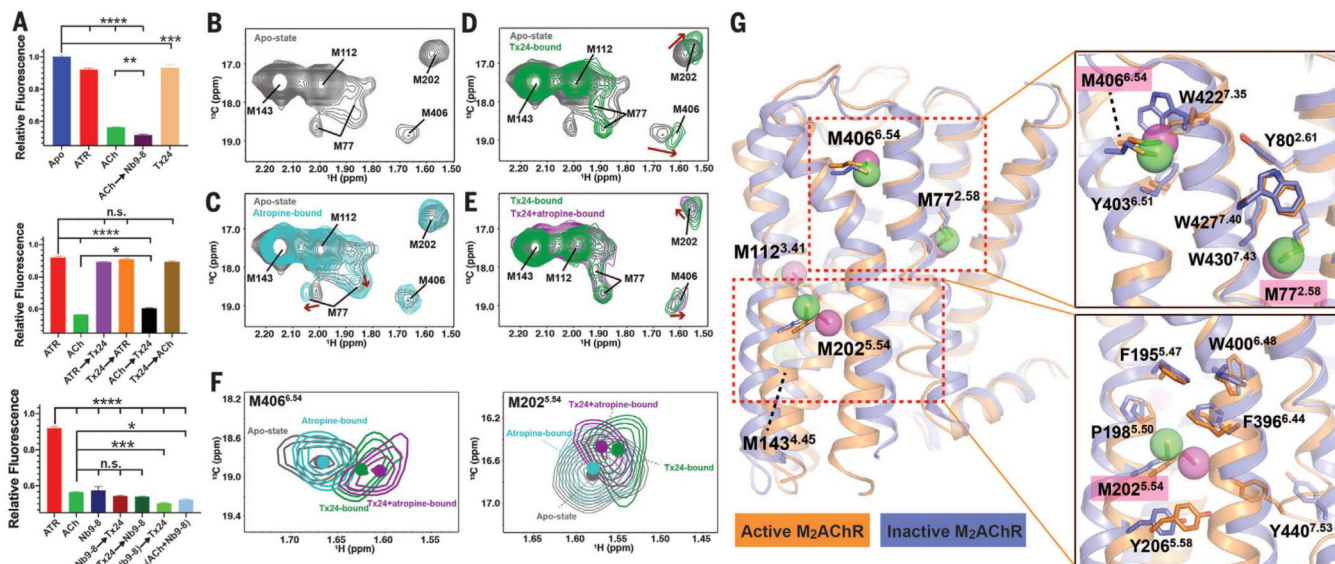
Fig. 6. Structural impact of Tx24 on M$_2$AChR conformation dynamics.
(**A**) Comparison of the fluorescence intensity of the mBBr-labeled M$_2$AChR in various conditions. Receptor was first incubated with the compound or protein listed first and then further incubated with the second molecule(s) before fluorescence spectra were obtained. Fluorescence peak intensities at 461 nm are plotted. Data represent at least three independent measurements. $*P < 0.05$; $**P < 0.005$; $***P < 0.001$; $****P < 0.0001$; n.s., not significant (one-way analysis of variance). (**B** to **E**) Structural impact of Tx24 on the HSQC spectra of the apo state, atropine-bound state, Tx24-bound state, and Tx24+atropine-bound state of M$_2$AChRmini$_\Delta$5M. (**F**) Overlay of spectra for M406$^{6.54}$ and M202$^{5.54}$ in different conditions from panels (B) to (E): apo state (gray), atropine-bound (cyan), **T**x24-bound (green), **T**x24+atropine–bound (magenta). The centers of the resonances are indicated with dots. (**G**) Distribution of methionine probes with the structural comparison between inactive (blue; PDB ID 3UON) and active M$_2$AChR (orange; PDB ID 4MQS). Side-chain interactions surrounding M406, M77, and M202 are detailed in the right panels.